DOE/MC/29061-96/C0662

CONF-9510109--38

Advanced Combustion Technologies for Gas Turbine Power Plants

Author:

Uri Vandsburger
Larry A. Roe
S. B. Desu

Contractor:

South Carolina Energy Research and Development Center
Clemson University
Clemson, SC 29634

Contract Number:

DE-FC21-92MC29061
Subcontract No. 93-01-SR013

Conference Title:

Advanced Turbine Systems Annual Program Review

Conference Location:

Morgantown, West Virginia

Conference Dates:

October 17-19, 1995

Conference Sponsor:

U.S. Department of Energy, Office of Power Systems Technology,
Morgantown Energy Technology Center

Contracting Officer Representative (COR):

Norman Holcombe

Disclaimer

P7

Advanced Combustion Technologies for Gas Turbine Power Plants

Uri Vandsburger (uri@stnick.me.vt.edu; (540)-231-4459)
Randolph Hall, 0238
Department of Mechanical Engineering
Virginia Tech
Blacksburg, VA 24061

Larry A. Roe (lar@engr.uark.edu; (501) 575-3750)
Department of Mechanical Engineering
University of Arkansas

S. B. Desu (desu@vt.edu; (540) 231-6640)
Department of Materials Science and Engineering
Virginia Tech
Blacksburg, VA 24061

1. Introduction

During the second half of fiscal year 1995 progress was made in all three funded subject areas of the project as well as in a new area. Work in the area of mixing and combustion management through flow actuation was transferred into an enclosed facility. Jet mixing in a ducted co-flow was examined. The same jets were also subjected to a strong acoustic field established in the duct. Excitation of the jet with static spatial modes was shown to be effective even in the presence of co-flow and the acoustic field. Only when a (reflective) wall is placed at the jet exit plane did the acoustic field dominate the jet dispersion (as expected due to reflective boundary conditions and the jet shear layer receptivity). This case is, however, not the most relevant to gas turbine combustors since it precludes co-flow. In the area of combustor testing, the design, fabrication, and assembly of a mudular combustor test rig for the project has been completed at the University of Arkansas. In the area of high temperature piezoceramic actuator materials development, $Sr_2(Nb_xTa_{1-x})_2O_7$ powders have been synthesized, and bulk samples and thick films sintered. These materials have a curie temperature of about 1400 °C compared wtih 300 °C for the commercially available PZT. While at room temperature the new materials show a piezoelectric constant (d_{33}) which is a factor of 100 lower than PZT, at high temperatures they can exhibit significant action. A new area of non-linear, neural-net based, controllers for mixing and combustion control has been added during the second contract year. This work is not funded by the contract. Significant progress was made in this area. Neural nets with up to 15 neurons in the hiden layer were trained with experimental data and

Research sponsored by the U.S. Department of Energy's Morgantown Energy Technology Center, under subcontract 93-01-SR013 (through South Carolina Energy R&D Center) with Virginia Tech, Blacksburg VA 24061-0238; fax: 540-231-9100

also with data generated using linear stability theory. System ID was performed successfully. The network was then used to predict the behavior of jets excited at other modes not used for the training. Work plans for the first half of the third year call for:

- development of improved passive and active schemes for rapid mixing,
- testing of the new piezoceramic materials in a high temperature environment, including the University of Arkansas combustor,
- fabrication of thick and thin films, and
- make progress towards a Neural Net mixing and combustion controller.

2. Objectives

The overall stated objectives for this project can be grouped into two categories:

- Development of actuation methodologies for enhancement of mixing between gas streams, and the increase of combustion stability.
- Development of high temperature materials for use as actuators and sensors in combustor environments.

For the second year, the specific goals set were:

- Examination of the utility of spatial mode excitation in ducted jets subject to an acoustic field.
- Synthesis of high temperature piezo-ceramic powders, and sintering of bulk materials and thick films.

Both goals have been fulfilled in a satisfactory manner.

The objectives for the third year include:

- Combustor testing of high temperature piezoelectric
- Development of new passive-active mixing enhancement methodologies based on simple concepts.
- Development of Neural Network based controllers for mixing and combustion stability.

3. Project Description

3.1 Non-Reacting Jets with Co-Flow in a Noisy Enclosure

3.1.1 Introduction. After the successful demonstration of spatial mode actuation, static and dynamic, on free jets, the next step was the examination of these methods on jets with co-flow in an enclosure. Since gas turbine combustors typically also exhibit a lively acoustic environment it was decided to examine the robustness of the spatial mode actuation scheme in the presence of an acoustic field generated by a pair of loudspeakers exciting the first transverse mode.

3.1.2 Experimental Equipment and Setup. Since the last report, additional hot-wire measurements have been performed to obtain information concerning the effect of various acoustic fields on the developing jet flow. The experimental setup is shown in Figure 1. Depending on the different test conditions, time-averaged and phase-locked velocity and turbulence data have been acquired and processed. The turbulent kinetic energy maps presented in this report are an axisymmetric cut of the x=0 plane which can be used for scaling the mixing characteristics in the mixing layer.

To verify the credibility of the data from previous hot-wire measurements, smoke flow visualization with a laser sheet was carried out. A schematic of the flow visualization system is shown in Figure 2. The smoke was generated by electrically heating mineral oil. Flow field pictures were taken with a Stanford Computer Optics 4 Quik 05 intensified CCD camera. A PC

486 computer was used to control the camera for image acquisition and image processing.

The flow conditions for the visualization tests were identical to those of the hot-wire tests, i.e. jet velocity U_j = 15 m/s, with a corresponding Reynolds number of 10,000, co-flow velocity U_{coflow} 3 m/s, and a simulated overall equivalence ratio ϕ = 0.45. In the case of the excited jet, a spatial mode excitation has been applied with m=+-1 and excitation frequency of 70 Hz.

Both longitudinal and transverse acoustic modes have been introduced into the duct to examine their effects on the jet flow. The longitudinal acoustic mode was the preferred mode of the jet shear layer, with a frequency of 210 Hz and a sound pressure level of 105 dB at the anti-node. Since the jet flow field appeared to be more sensitive to the transverse acoustic mode than to the longitudinal mode, emphasis was placed on the investigation of the effect of the transverse resonance mode on the flow field. The first transverse mode of the duct has a frequency of 1335 Hz and a SPL of 125 ~ 136 dB at the anti-node).

3.2 Development of Neural Network Based Controllers

3.2.1 Motivation and Objectives. A new aspect of the program was initiated this year addressing the development of non-linear control strategies for mixing and reacting shear flows. This effort involves an additional faculty member from the department of mechanical engineering, Dr. William Saunders, and a graduate student, both not supported by the project. Due to the inherent non-linear nature of fluid flow systems, neural network based systems seem very attractive.

Research at Virginia Tech has already investigated and identified actuation schemes which are highly beneficial for the mixing of initially separate fluids (Vandsburger and Ding, 1994). The main objective of this research is to explore the possibilities of applying nonlinear control methodologies, e.g., neural networks, as part of a complete control system for jet flows, both non-reacting and reacting.

To fully realize the potential of these control techniques in shear flows and practical combustion devices, the research has been divided into three distinct stages:

I. Construct a neural network model of the near and far field structure of spatially excited jets.

II. Develop a neural network adaptive controller to optimize air/fuel mixing.

III. Apply the concepts developed in stages I and II to reacting shear flows in order to optimize combustion.

Thus, the research is focused around increasing volumetric heat release rate by maximizing air/fuel mixing.

3.2.2 Neural Network Modeling of Spatially Excited Jets. Traditional control strategies are able to predict cause and effect relationships upon a particular system with the use of a mathematical model that describes the physics of the process involved. Most often a differential equation is the underlying model used to describe the dynamics of such a system. For example, in the conventional spring/mass/damper system, the differential equation is ordinary, linear, and of closed form. However, the equations governing the dynamics of fluid flow (Navier-Stokes), are not as easily solved, even when gross assumptions are made. However, by choosing an artificial neural network (ANN) as the mathematical model for the control scheme, the difficult and often futile task of identifying the exact physics involved in a complicated reacting flow is surpassed. Neural networks can be highly nonlinear by design and are able to establish complex relationships between multiple inputs and outputs by learning from experimental data. Essentially, the

differential equation describing the physics of the problem is replaced by the experimentally-based ANN model. A simple example of such system identification using neural networks is illustrated in Figure 3. In Figure 3, the teacher represents the actual system based upon an experimental data set of input (x(t)) and output (f[x(t)]) examples, and the object of the neural network is to emulate the teacher by minimizing the error signal, e(t), between the two models.

The question now becomes whether experimental data can be used to emulate a jet undergoing spatial mode manipulation, as shown in Figure 4. The experimental actuation technique which was used to generate such iso-velocity contours involved the use of acoustic actuators placed around the exit of a jet. This arrangement allowed the excitation of various azimuthal (spatial) modes which affect the cross-sectional size and shape of the iso-velocity profile downstream from the nozzle exit. Here, the inputs to the system identification diagram are the actuation signals to the loudspeakers, and the outputs are the iso-velocity contour data. Once the ANN is trained to emulate the jet, the neural network could then be given an untrained actuator signal for which it would anticipate the flow field evolution. Figure 5 illustrates an example of this, where the ANN models a jet undergoing +/-2 mode excitation. Both linear and non-linear neural networks were used to generate the velocity profiles for a normalized velocity contour of 0.3 at three distances downstream of the jet exit (x/D = 3.5, 4.5, 5.5).

Spreading rates for different spatial mode excitations can also be approximated by the ANN as shown in Figure 6. In Figure 6, the ANN was not trained on experimental data for modes +0.5 and +0.75, yet it still generalizes well to give a reasonable estimate of spreading. By anticipating such aspects of the flow field from specified actuator control signals, the ANN-generated flowfield model will ultimately serve as the foundation upon which to build an adaptive control system.

3.3 Medium Scale Combustor at University of Arkansas

As part of the ATS project, a medium scale combustor test rig was to be constructed at the university of Arkansas, department of mechanical engineering. The test system is to be capable of evaluating actuated combustor methodologies at realistic scales, temperatures, and acoustic environments. The fuel is natural gas; either premixed of non-premixed operation is available. The first series of experiments will evaluate flame stabilization and will operate in the premixed mode. The acoustic environment is provided by external acoustic drivers, with controlled amplitude and spectral content. Intrinsic background noise levels in the air supply system are minimized to provide controlled conditions in the combustor section. A 500 CFM Gardener-Denver Cycloblower was chosen for the primary air supply because of the very low pressure fluctuations associated with this helical screw design. During this reporting period, the air supply system was designed, the blower was specified, purchased (with non-contract funds) and installed, and acoustic analyses of the air supply ducting, fuel/air mixer, flow straiteners, and flashback arrestor were conducted. The analyses show a predicted background noise level of 85 dB, well below the level capable of being produced in the test section by external drivers. Assembly of the air supply system is approximately 80 percent complete.

For premixed operation, a fuel injection and mixing section ensures complete mixing of the fuel and air with a minimum reactive volume and a minimum residence time. Using a simplified Fluent CFD model, a radial spoke, multipoint fuel injector scheme and a cross-flow (cone) mixer were designed. The model is

currently being refined to more accurately predict the fuel-air mixing.

A preliminary design of the test section and combustor has been completed. The initial testing will be of an axisymmetric, centerbody-stabilized, premixed combustor, which models many of the stabilization characteristics of proposed ATS designs. The centerbody will incorporate piezoceramic shear layer actuators and will be similar in design to the nozzles used for actuated jet mixing studies at Virginia Tech, although the actuators themselves will be manufactured from the new materials being developed under the materials portion of this contract at Virginia Tech. This will provide for the evaluation of the actuators under full temperature conditions. The quartz test section will provide full optical access for shadowgraph and emission photography.

During this period, existing gas analyzers were evaluated and checked for proper operation. The analyzers available are a Thermo Electron Model 10A chemiluminescent analyzer for NO_x, two Beckman Model 315A(S) NDIR analyzers for CO and CO_2, and a Beckman Model 400 FID hydrocarbon analyzer. The NO_x analyzer has been fully checked out and is in working condition. The CO and CO_2 analyzers passed the initial tests but are currently missing calibration curves for some ranges. The hydrocarbon analyzer is considered a low-priority diagnostic device and has not yet been evaluated.

3.4 Fabrication and Property Measurement of High Temperature Piezoelectric Materials

3.4.1 Overview. Due to the high temperatures encountered in a reacting flow, the piezoelectric materials to be used in a combustor must possess high Curie-temperatures. $A_2B_2O_7$ materials like $Sr_2(Nb_xTa_{1-x})_2O_7$ and $La_2Ti_2O_7$ were chosen to satisfy the high Curie-temperature requirements. Compared to conventional actuator materials, for example PZT, $[Pb(Zr_xTi_{1-x})O_3]$, the new piezoelectric materials have lower dielectric constants and piezoelectric coefficients at room temperature, but exhibit extremely high Curie-temperatures. Conventional piezoelectric materials are not suitable for high temperature applications due to their lower Curie temperature (e.g. PZT, Curie temperature≈ 300°C). Table 1 shows a comparison between the new material, $Sr_2(Nb_xTa_{1-x})_2O_7$ and the conventional material, $Pb(Zr_xTi_{1-x})O_3$.

During this reporting period, $Sr_2(Nb_xTa_{1-x})_2O_7$ thick films were prepared by the tape-casting method. X-ray diffraction patterns were used to identify the single phase formation, and their piezoelectric properties were measured by a d_{33} meter.

There are three possible types of piezoelectric ceramic actuator designs: multilayers, bimorphs, and the Moonie structure. The characteristics of the different ceramic actuators are summarized in Table 2. The multilayer actuator exhibits large forces and small displacements, whereas the bimorph actuator generates small forces and large displacements. The Moonie structure actuator, shown in Figure 7, is a reasonable compromise capable of sizable forces and appreciable strains. The piezoelectric coefficient for the Moonie structure actuator was found to be larger than without the Moonie structure.

3.4.2 Experimental Approach and Technique. A flow chart outlining the preparation of the thick film is shown in Figure 8. Reagent-grade (purity 99.9%) component oxides in their respective mole ratios were mixed for 24 hours in a crucible including alumina media and alcohol. The resulting slurry was dried at 150°C and calcined at various temperatures for 3 hours to obtain the single-phase. The calcined powders were ball-milled again in an organic binder solution for 24 hours. The amount of binder and solvent was adjusted

by viscosity of the mixed slurry. The binder contains polyvinyl butyral (PVB) polymer, a plasticizer, a surfactant, and an ethanol+toluene solvent. Samples were prepared by casting the slurry using a scalpel. The thick films were formed on silicone coated mylar sheets for easy peel-off. The process of drying the films was followed by a binder removal procedure: heating up to 500°C for 3 hours and holding at 500°C for 2.4 hours. Then, the thick films were sintered at various temperatures ranging from 1200°C to 1500°C.

3.4.3 Moonie Actuator. The composite actuators consist of piezoelectric ceramics and brass-end caps. A shallow cavity, as shown in Figure 7, was made in the center of the brass cap. The brass-end caps were attached to the piezoelectric ceramic using silver paste. Special care was taken not to fill up the cavity, or short circuit the ceramic electrodes. The stacked composite was heated at 150°C under stress to solidify the bond. An epoxy resin was pasted around the circumference to encapsulate the actuator.

Because the polarization inside the ceramics is randomly oriented, the piezoelectric ceramics do not exhibit their piezoelectric properties until a high DC voltage is applied to the sample. The polarization is forced to be aligned in the direction of the applied DC voltage. This process is called poling.

When a sample is poled, an insulating material is needed because of the very high applied voltage (more than 2MV/m). Silicon oil is typically used as the insulating material. By increasing the temperature of the silicon oil bath, the polarization can be more easily switched to the direction of the applied voltage. However, the elevated temperature must be kept below the Curie temperature or the samples lose their piezoelectric properties. In the present experiments, the samples were poled at 3MV/m for 15 min. in a silicon oil bath held at 200°C. The direct piezoelectric coefficient was measured at a frequency of 60 Hz using a d_{33} meter.

4. Results

4.1 Non-Reacting Jets with C0-Flow in a Noisy Enclosure

The turbulent kinetic energy maps of an excited jet with co-flow in a cavity with a partially closed exhaust end are shown in Figure 9 and Figure 10 for cases with and without the imposition of a longitudinal acoustic field, respectively. The results show very little change in the flow field, which implies that any coupling from the longitudinal acoustic field is unable to compete with the perturbation from the actuators. Other explanations could be the protective effect of the co-flow layer or the relatively low sound pressure levels due to the unrestricted co-flow inlet, the absence of a reflective boundary condition at the jet exit (no end plate).

A time-averaged turbulent kinetic energy map of an unexcited jet in a cavity with a closed co-flow inlet and a partially closed exhaust end is shown in Figure 11 while the phase-mean data of the same jet subject to an imposed transverse acoustic field in the same cavity is shown in 12. It is seen that under the imposition of the acoustic field, the shear layer thickness increases and the potential core length decreases.

Similar results can be found in Figure 13 and Figure 14, which are the phase-mean turbulent kinetic energy maps of an excited jet in a cavity with a closed co-flow inlet and a partially closed exhaust end, with and without an imposed transverse acoustic field, respectively. Although the turbulent kinetic energy distribution is affected by the acoustic field both in space and time, the basic flow features

resulting from spatial modulation obviously remains unchanged.

The test duct inlet condition became a major focus of these experiments since it strongly influences the response of the jet flow to the imposed acoustic field. The effects of the co-flow and duct exit cross sectional area were also investigated.

The flow visualization images of ducted jet flow for different inlet conditions are shown in Figure 15. When exposed to the acoustic field, the jet seems to expand relatively faster when the co-flow is stabilized by a wall. In comparison, the jet expansion does not change in an obvious manner in the absence of that wall. This result implies that the acoustic boundary conditions near the jet shear layer strongly influence the impact of an imposed acoustic field. The effect of an acoustic field in a combustor on the fuel mixing will therefore depend on the design of the fuel injection region.

The influence of the end nozzle on the coupling between the acoustic field and the developing flow field looks minimal as shown in Figure 15. The reason appears to be that the end nozzle was located at the opposite side of the loudspeakers with respect to the examined jet and thus the existence or not of the end nozzle had only a negligible influence on the sound pressure level near the jet shear layer.

The images of an unexcited jet subject to a imposed transverse acoustic field in the cases of with and without co-flow are shown in Figure 17. Similar to what was found in previous studies, the co-flow tended to attenuate the effect of acoustic field on the jet flow. The small effect may also be attributed to unrestricted co-flow inlet.

4.2 Medium Scale Combustor: University of Arkansas

At this time, the blower is mounted in place and a delivery date for the 25-hp drive motor and variable speed controller has been set. The duct supports, flow straiteners, and flashback arrestor are complete. The pipe sections and miscellaneous components (interconnects, fittings, gaskets, etc.) are on hand. The mixing cone has been received and is ready to be machined and installed.

Installation of a 5 psig natural gas supply line (with non-contract funds) was recently completed. Work is in progress on the remainder of the fuel supply system; the fuel injection ring fabrication is awaiting final results from the fluent analysis. All necessary gas analysis and optical instrumentation is in place.

4.3 High Temperature Piezoelectric Materials

The $Sr_2(Nb_xTa_{1-x})_2O_7$ (x=1.0) ceramics prepared by the chemical coprecipitation method (CCP) were cut along a-axis, b-axis, and c-axis as shown in Figure 18 to investigate the anisotropy in electrical properties. The dielectric properties were measured at a frequency of 10 kHz for a $Sr_2(Nb_xTa_{1-x})_2O_7$ sample sintered at 1500°C. The results of the electrical properties of $Sr_2(Nb_xTa_{1-x})_2O_7$ (x=1.0) ceramics prepared by the CCP method and the conventional method (CON) are summarized in Table 3. The dielectric constant of the a-cut sample is higher than that of the single crystal. The microstructures of the samples cut along the three axes are presented in Figure 19. The orientation of grains can be clearly observed in the a-cut and b-cut samples, whereas the grains in the c-cut sample seem to be randomly oriented.

Dielectric constants of $Sr_2(Nb_xTa_{1-x})_2O_7$ ceramics were plotted as a function of temperature as shown in Figure 20. The Curie temperature increased with the composition, x. Relative permitivity at Curie temperature and grain orientation are shown in Figure 21. The value of grain orientation is proportional to the composition.

The d_{33} coefficient expresses the ratio of the strain developed in a piezoelectric ceramic to the applied field: $\varepsilon_{ij} = d_{ijk}E_k$, where ε_{ij}, d_{ijk}, and E_k represent mechanical strain, piezoelectric coefficient effect, and electric field, respectively. It is also related to the ratio of the voltage developed by a ceramic for an applied stress. As such, it determines the "sending" and "receiving" characteristics of a ceramic, and is one of the most important coefficients to know when evaluating piezoelectric materials. The d_{33} coefficients were measured at room temperature for $Sr_2(Nb_xTa_{1-x})_2O_7$ ceramics, and were plotted as a function of composition, x, in Figure 22. The $Sr_2(Nb_xTa_{1-x})_2O_7$ ceramics (x=0.2 and 0.4) with relatively low Curie-temperatures showed larger d_{33} values than the ceramics with the compositions x=0.8 and 1.0. The value of d_{33} coefficient is inversely proportional to the composition. It has to be stressed again that the d_{33} values were measured at room temperature. They are expected to increase by close to 100 at higher temperatures.

The d_{33} piezoelectric coefficient was measured by using a d_{33} meter on various samples: the bulk ceramics prepared by conventional method (CON), molten salt method (MSS), and chemical coprecipitation method (CCP), and the thick films. Generally, the d_{33} value of the thick films is higher than that of the bulk samples. Among the bulk ceramics, the sample prepared by the CCP method exhibited a little larger d_{33} coefficient than the sample prepared by CON and MSS methods.

Moonie structure actuators were fabricated by using $Sr_2(Nb_xTa_{1-x})_2O_7$ (x=1.0) ceramics prepared by MSS method, and their piezoelectric coefficients were measured, again at room temperature. The value of the d_{33} coefficient increased from 1.4 pC/N to 1.9 pC/N by using the Moonie-structure design. The Moonie structure actuator improves the d_{33} coefficient by adding the d_{31} coefficient to the d_{33} coefficient. When an electric field is applied to a sample, the piezoelectric ceramic extends longitudinally through d_{33}, and contracts transversely through d_{31}. In the Moonie structure actuator, the radial motion of the ceramic is transformed to the flextensional motion of the brass caps. Therefore, the axial displacement comes from two different sources. One is the longitudinal displacement of the ceramic itself through d_{33}, and the other is the flextensional motion of the metal arising from the transverse contraction through d_{31}. The two contributions add together to give overall larger displacements.

5. Activities Planned for Year 3

5.1 Flow Control Area

After the proven success of spatial mode excitation of free and enclosed jets the realization of these methods in practical devices has to be considered. The practical realization of piezoceramic-based jet flow actuation has to overcome two hurdles, one the proof or reliability of moving/vibrating parts, and the availability of appropriate materials. The second part has been addressed through the development of high curie temperature piezoceramic materials discussed in section 3.4.

For practical reasons industry will be skeptical of mixing control relying on moving parts, even if it is the only scheme offering real control. For this reason a compromise solution will be sought during the coming period. The solution will be based on two approaches.

1) Combine passive mixing regulation with a minimum of active elements.
2) Develop an active mixing control system where the number of actuators is minimized.

Both approaches will be tested on experimental hardware which has already been set up in the Reacting Flow Lab at Virginia Tech. Both schemes will be developed and tested for open/free and enclosed/ducted jets, including the subjection to a noisy environment.

5.2 Neural Network Controller for Optimization of Air/Fuel Mixing

Once the jet is modeled correctly, a second neural network can be implemented to serve as a controller which adaptively optimizes air/fuel mixing. In addition to the ANN control algorithm, the proposed control system also includes actuators, sensors and actuation techniques developed at Virginia Tech. The loudspeakers and/or piezoelectric materials will serve as the actuators, and optical techniques will be employed as the sensors in order to feed-back the effectiveness of a particular actuation scheme on the mixing process. Using flow visualization will allow fast, quantitative analysis of two and three-dimensional iso-concentration contours in the flow field.

5.3 Combustion

At the University of Arkansas, the Fluent model results for the fuel injection and mixing section will be incorporated into the final fuel injector design. Machining of the fuel injector and mixer will be completed. The blower motor and speed controller, all remaining ductwork, and fuel supply lines will be installed and instrumented. Combustor design will be finalized and fabrication started. Initial hot testing with a generic, non-actuated combustor will be conducted to validate the operation of the air supply, fuel supply, and instrumentation.

New actuator materials will be tested in the combustor in early 1996. The setup will be one of an actuated bluff body stabilizer for lean, premixed, combustion.

5.4 Work in the Materials Area

The future work in materials development will focus on improving d_{33} coefficients of bulk ceramics and thick films. Large piezoelectric coefficient will be obtained by fabricating more dense and compositional homogeneous samples, increasing the temperature of oil bath, and applying higher electrical voltage. The following tasks will be carried out:

- fabricate thick films as a function of composition x,
- apply Moonie-structure design to the thick film,
- measure d_{33} coefficient at higher temperature,
- test several actuator geometries in high temperature environments at Virginia Tech and the University of Arkansas.

6. References

Gutmark , E., Parr, T.P., Parr, D.M., Schadow, K.C.,"Evolution of vortical structures in flames," Twenty-Second Symposium (International) on Combustion, 1988, p. 523-529.

Vandsburger, U., and Ding, C., "Spatial modulation of a forced triangular jet", Experiments in Fluids v 18 n 4 Feb 1995. p239-247.

7. Acknowledgement

The authors would like to acknowledge the continuous support of the SCERD staff, in particular Mr. Dan Fant and Larry Golan. Special thanks for enabling one of the students, S. D. Lepera, to spend a summer internship at Allison Turbine in 1995.

Table 1. The structural and electrical properties of $Pb(Zr_xTi_{1-x})O_3$ and $Sr_2(Nb_xTa_{1-x})_2O_7$.

	$Pb(Zr_xTi_{1-x})O_3$	$Sr_2(Nb_xTa_{1-x})_2O_7$
Structure family	Perovskite	Pyroniobate
Dielectric constant at room temperature	High	Low
Piezoelectric constant at room temperature	High	Low
Curie temperature	Low (≈ 300°C)	High (≈ 1400°C)

Table. 2. Types of piezoelectric actuators and their characteristics.

	Advantages	Disadvantages
Multilayer actuator	Low driving voltage Quick response High generative force	Low displacement
Bimorph actuator	Large displacement	Slow response Low generative force
Moonie-structure actuator	Sizable force and displacement	

Table 3. Electrical properties of $Sr_2(Nb_xTa_{1-x})_2O_7$ (x=1.0) sample sintered at 1500°C.

Method	Sample	Dielectric constant,ε (10 kHz)	Dielectric loss, tanδ (10 kHz)
CCP	a-cut	86 (75*)	0.0077
	b-cut	44 (46*)	0.0102
	c-cut	35 (43*)	0.0047
	disk type	49	0.0291
CON	disk type	52	0.0684

* indicates data from *Ferroelectric Properties of $Sr_2Nb_2O_7$ Single Crystal*

Table 4. d_{33} coefficients of $Sr_2(Nb_xTa_{1-x})_2O_7$ (x=1.0) ceramics and thick films at room temperature.

samples	method	d33 coefficient (pC/N)
Bulk ceramics	CON	1.0
	MSS	1.4
	CCP	1.7
Thick film		2.0

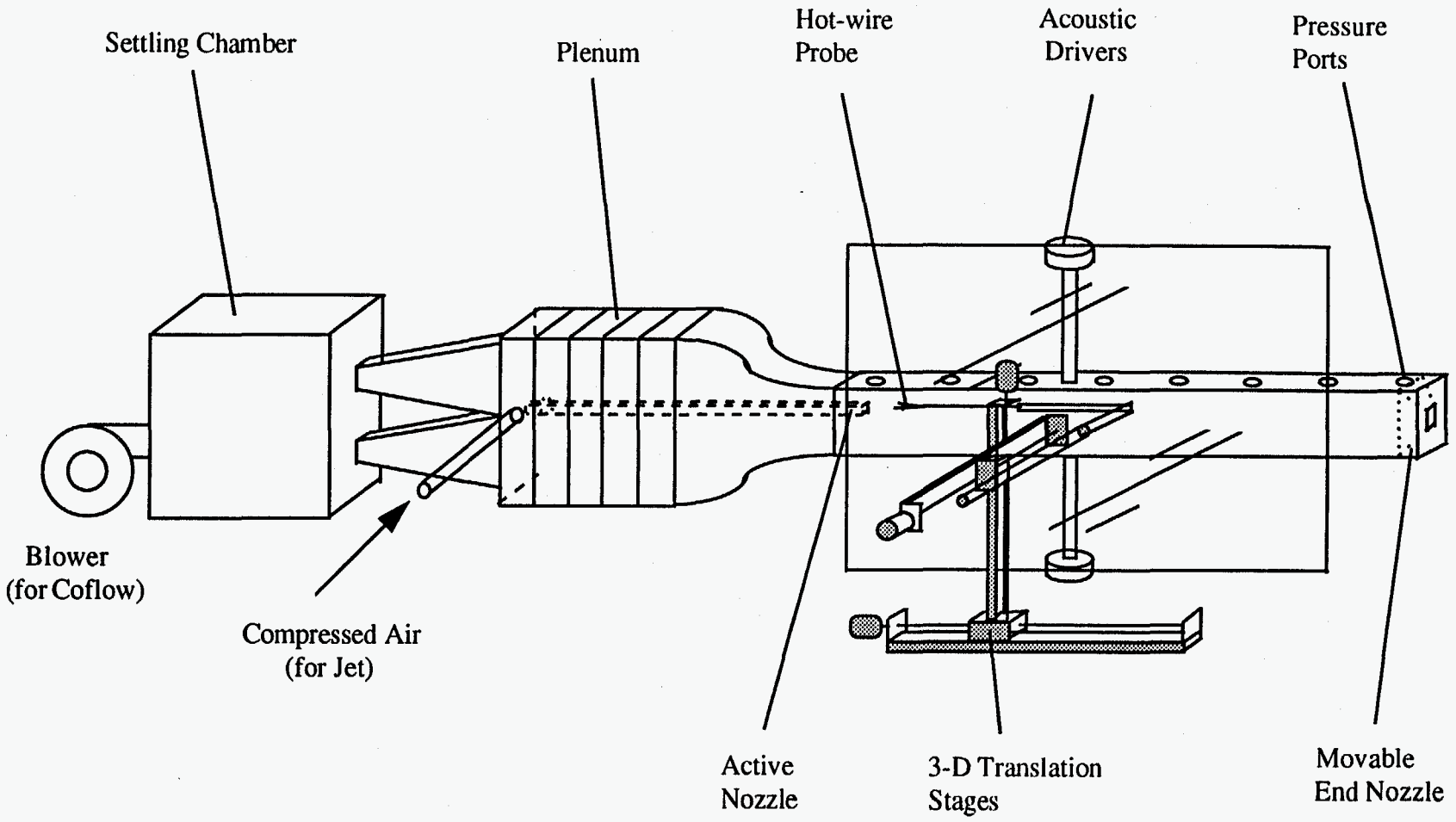

Figure 1. System setup for hot wire measurement

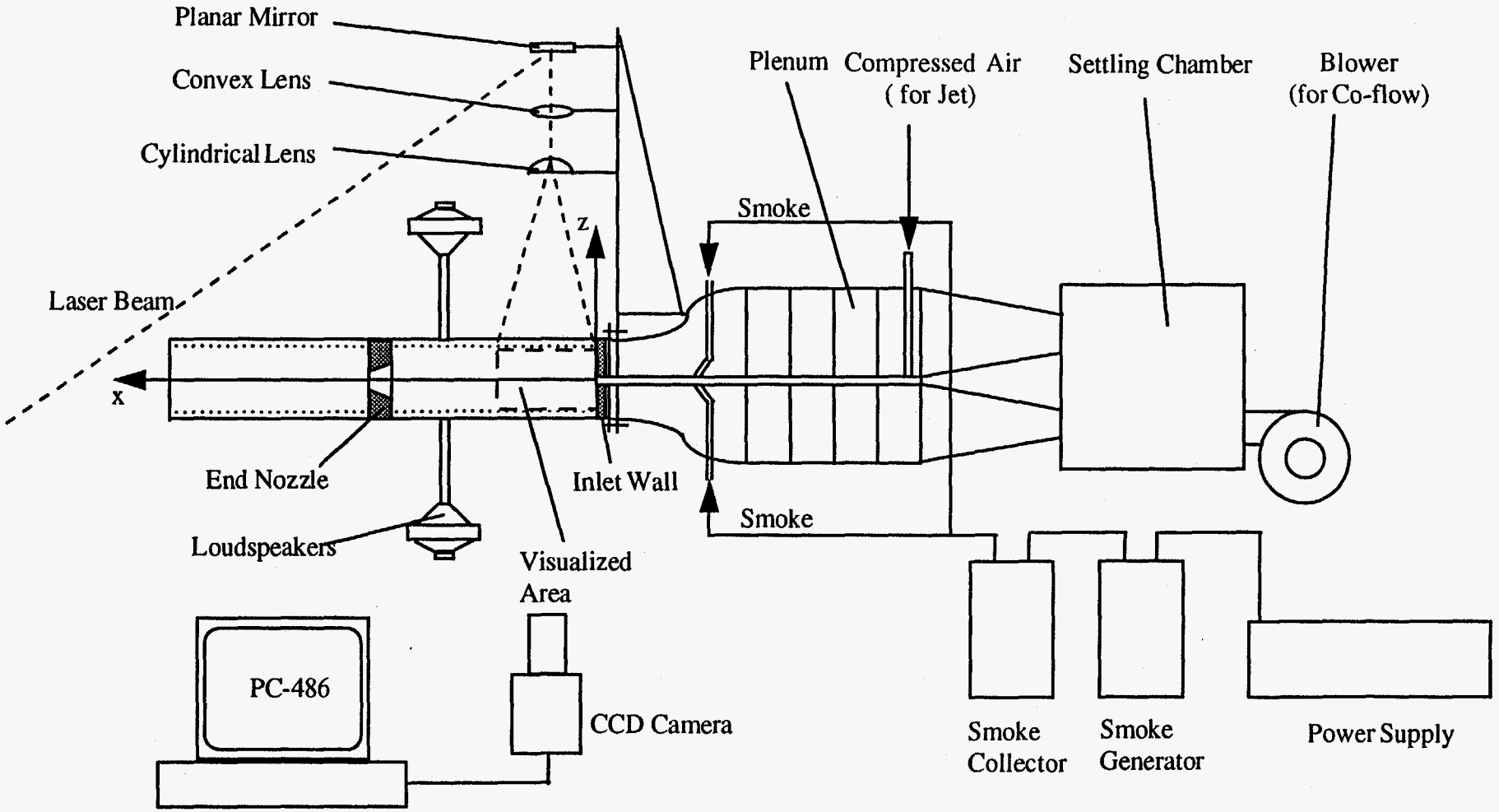

Figure 2. System setup for flow visualization

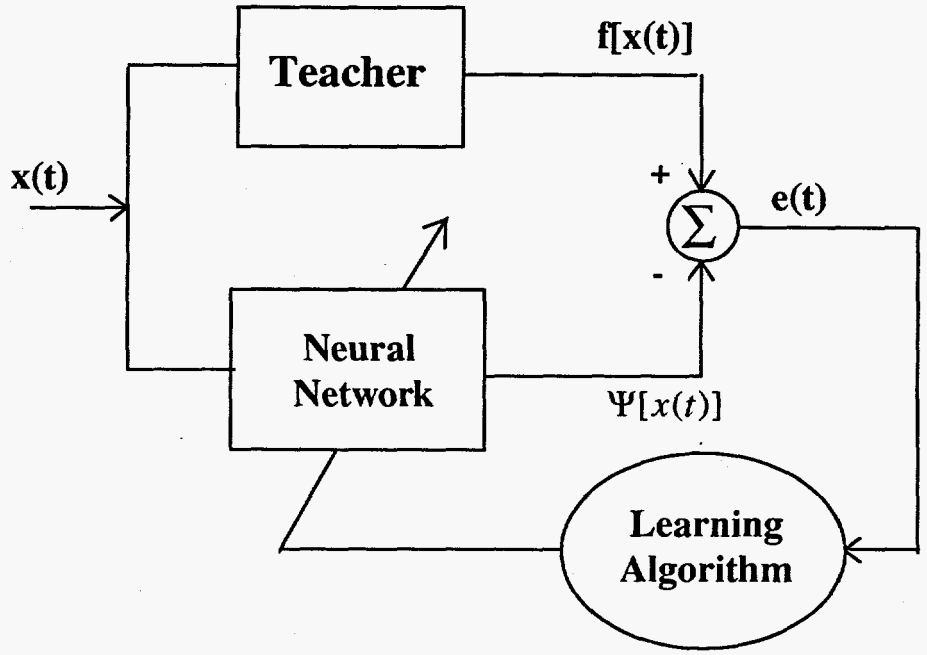

Figure 3. Modeling a system with Neural Networks

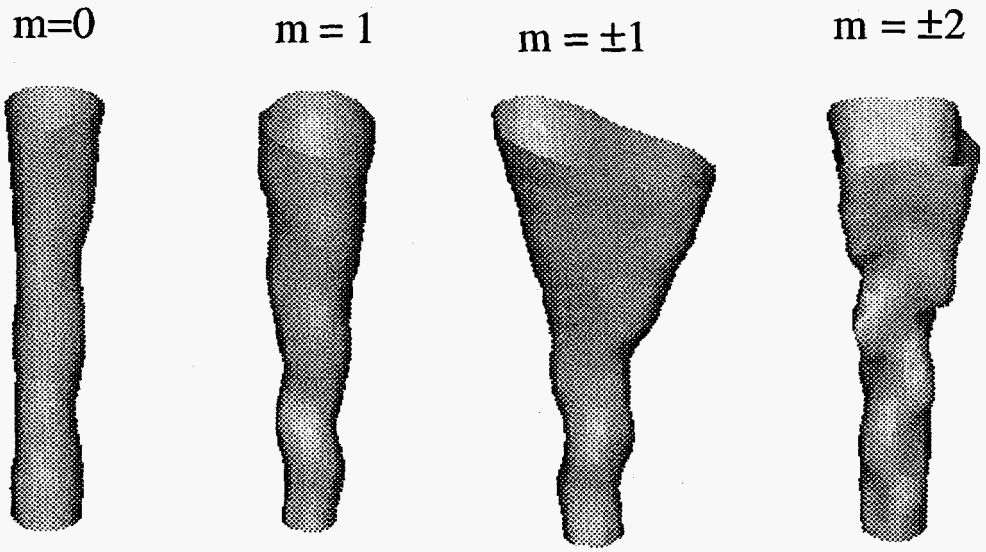

Figure 4. Iso-Velocity Contours of a Jet Undergoing Spatial Mode Manipulation

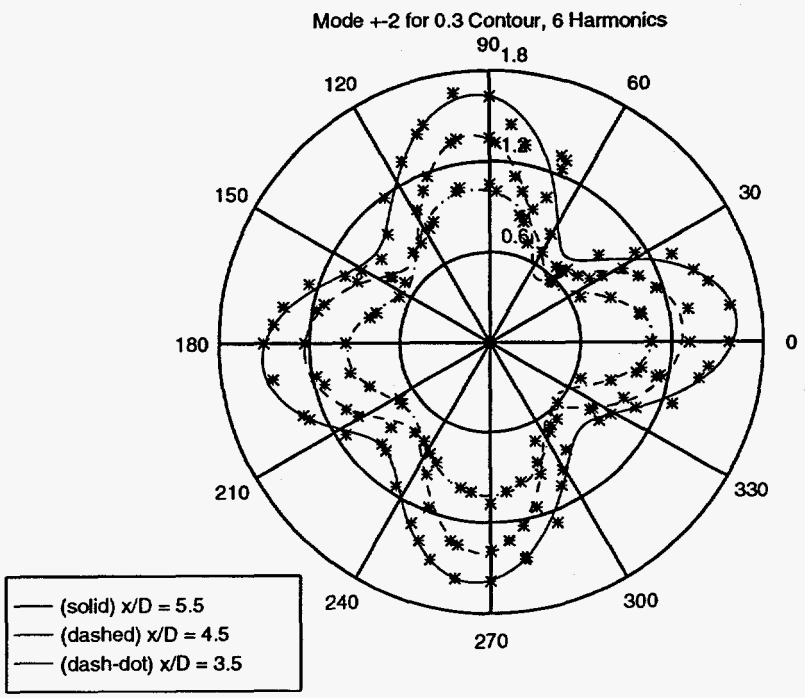

Figure 5. Approximation of velocity profiles for different distances (x/D) downstream of the jet exit

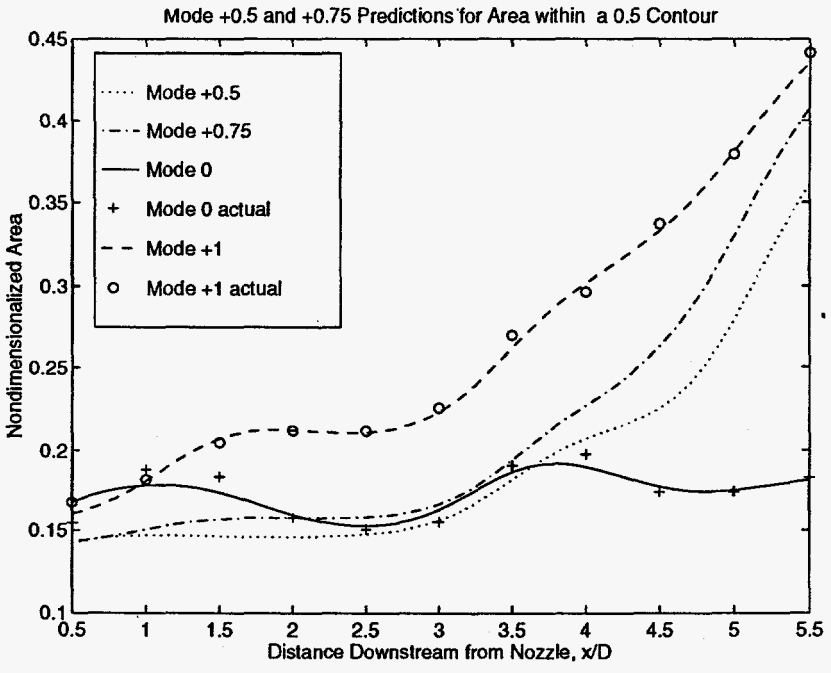

Figure 6. ANN Predictions for Jet Spreading Rates

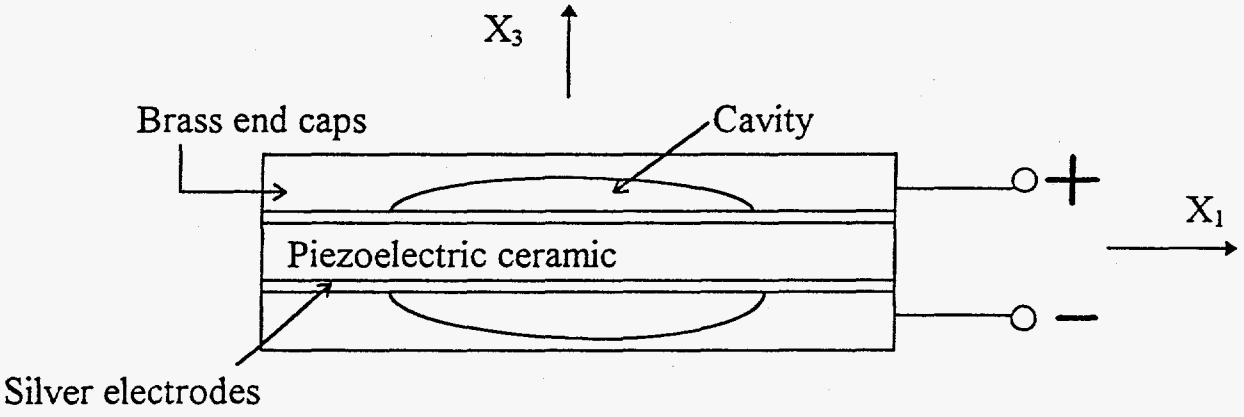

Figure 7. Design of Moonie structure actuator

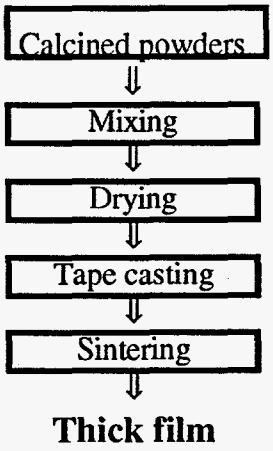

Figure 8. Schematic outline of tape-casting method for synthesizing piezoelectric thick film

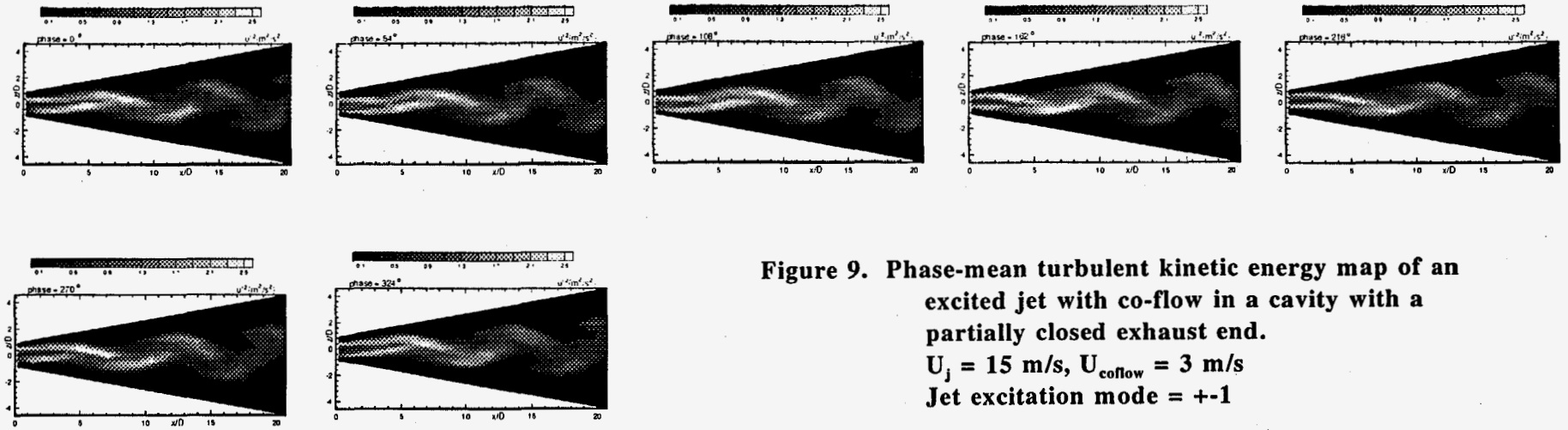

Figure 9. Phase-mean turbulent kinetic energy map of an excited jet with co-flow in a cavity with a partially closed exhaust end.
U_j = 15 m/s, U_{coflow} = 3 m/s
Jet excitation mode = +-1

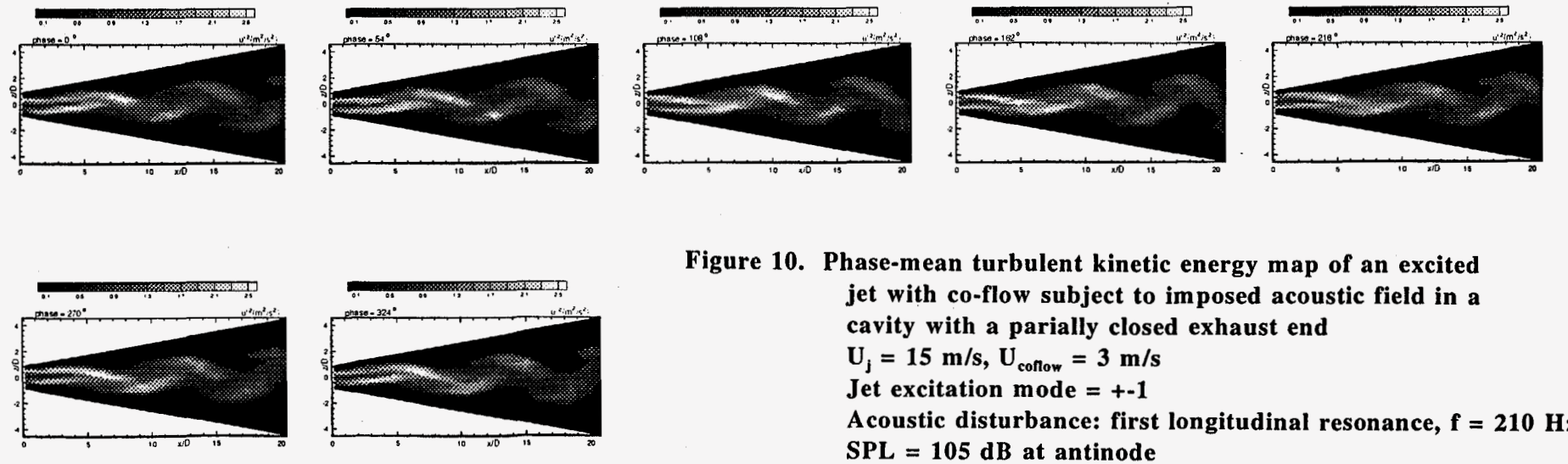

Figure 10. Phase-mean turbulent kinetic energy map of an excited jet with co-flow subject to imposed acoustic field in a cavity with a parially closed exhaust end
U_j = 15 m/s, U_{coflow} = 3 m/s
Jet excitation mode = +-1
Acoustic disturbance: first longitudinal resonance, f = 210 Hz
SPL = 105 dB at antinode

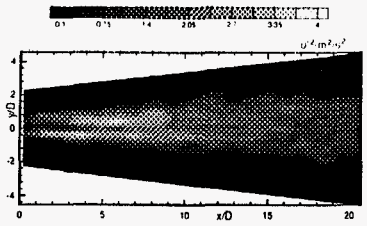

Figure 11. Time-mean turbulent kinetic energy map
unexcited jet
closed co-flow inlet
partially closed outlet
U_{jet} = 15 m/s

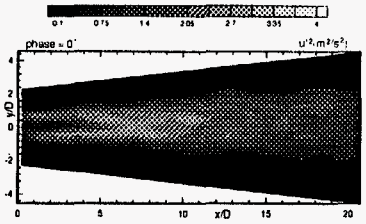

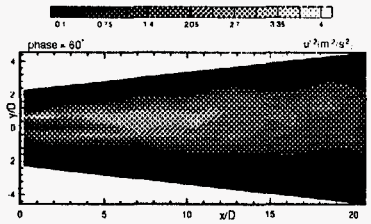

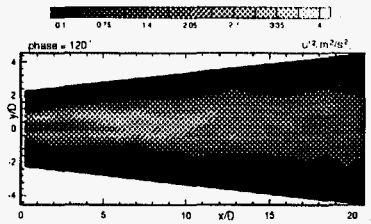

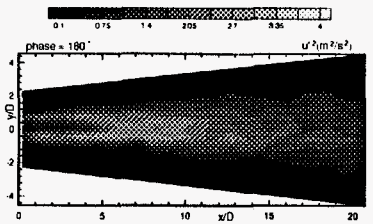

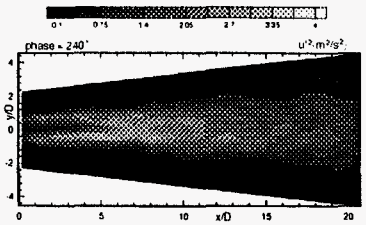

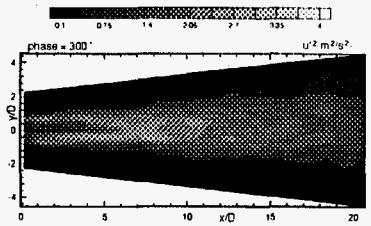

Figure 12. Phase-mean turbulent kinetic energy map
unexcited jet
Closed co-flow inlet
U_{jet} = 15 m/s
Acoustic disturbance: first transverse resonant mode, f = 1345 Hz, SPL = 125 dB at antinode

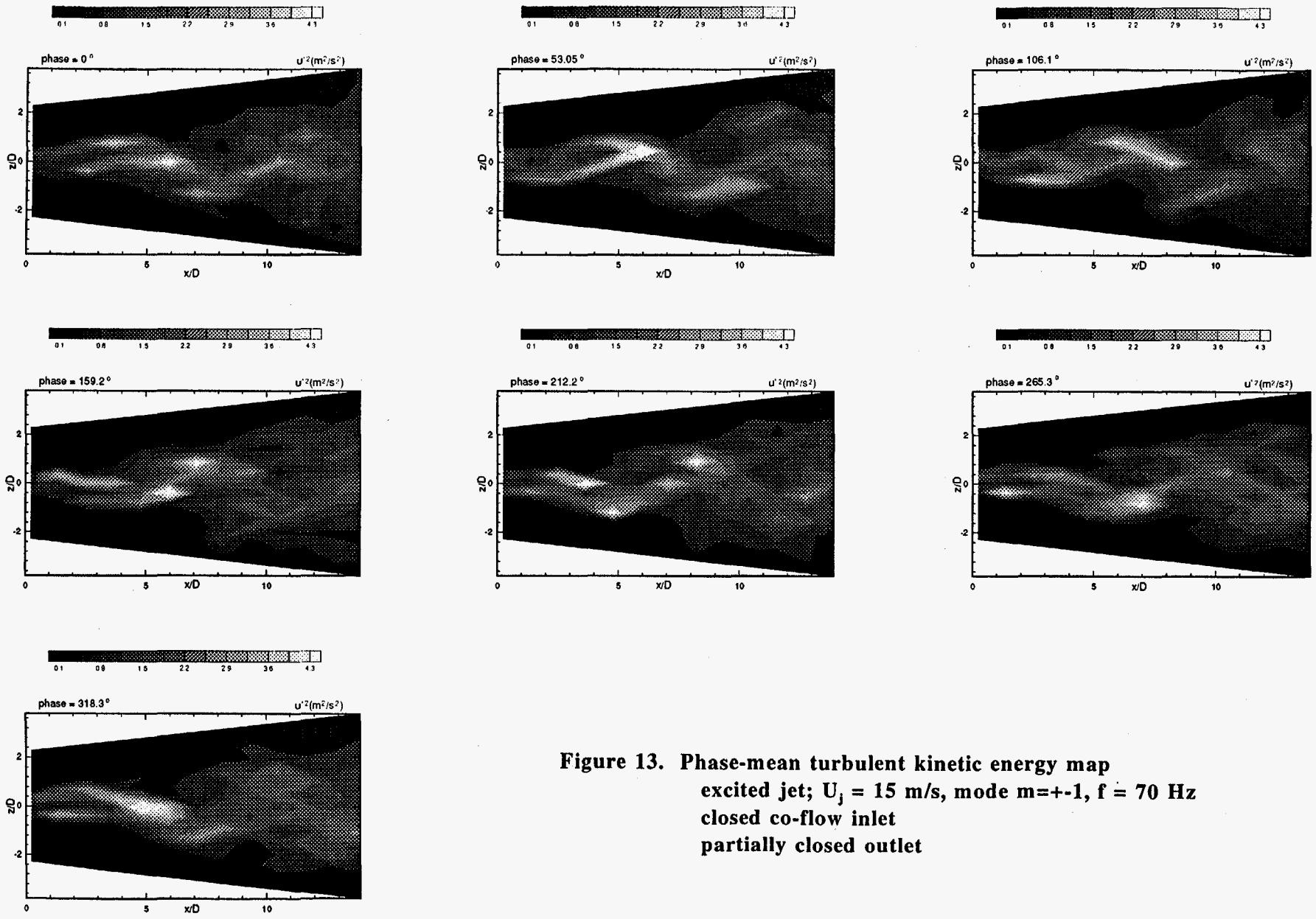

Figure 13. Phase-mean turbulent kinetic energy map
excited jet; U_j = 15 m/s, mode m=+-1, f = 70 Hz
closed co-flow inlet
partially closed outlet

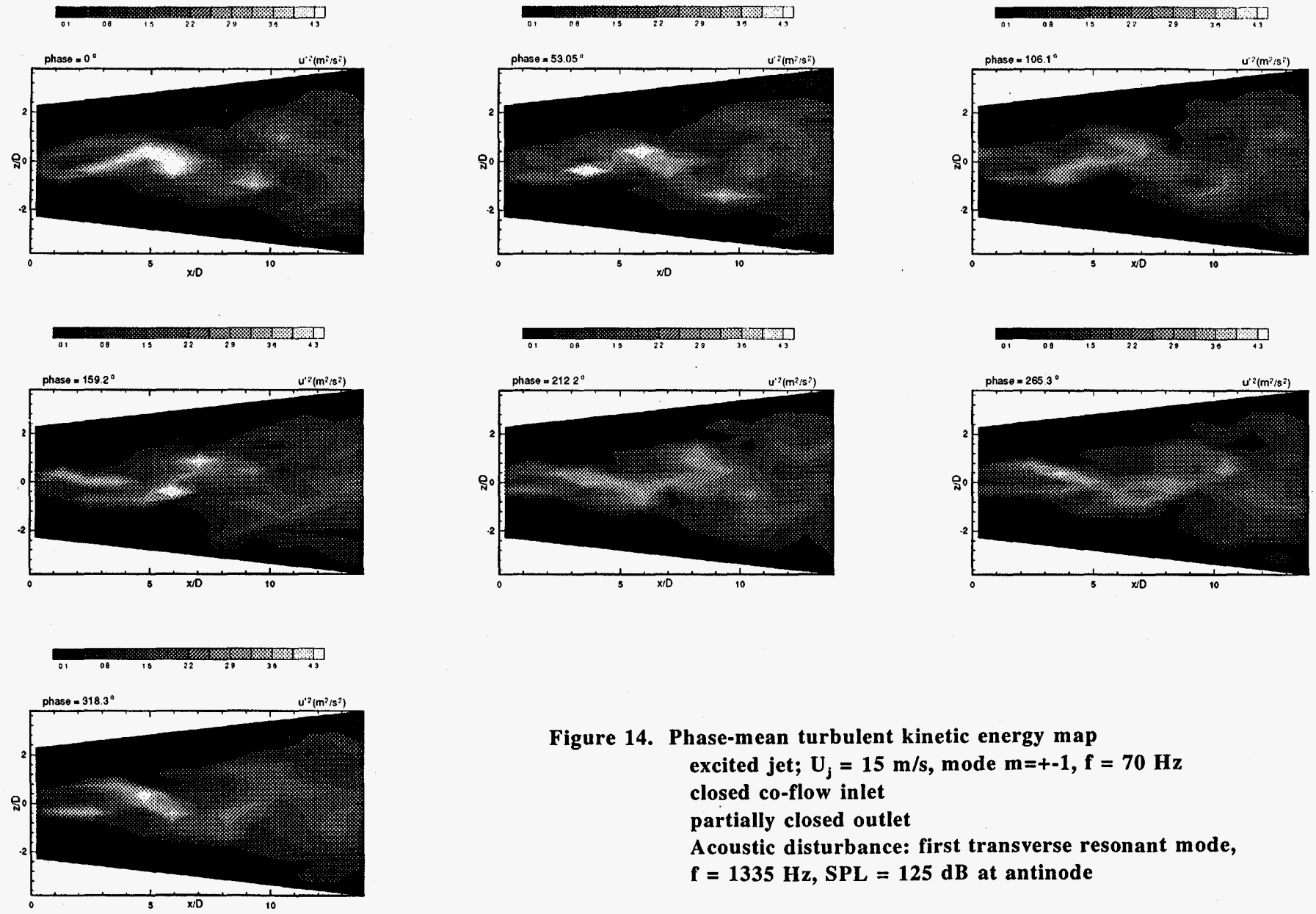

Figure 14. Phase-mean turbulent kinetic energy map
excited jet; U_j = 15 m/s, mode m=+-1, f = 70 Hz
closed co-flow inlet
partially closed outlet
Acoustic disturbance: first transverse resonant mode,
f = 1335 Hz, SPL = 125 dB at antinode

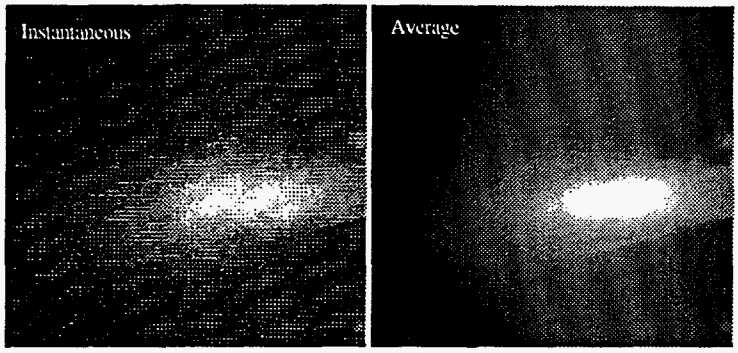

(a). No imposed acoustic field

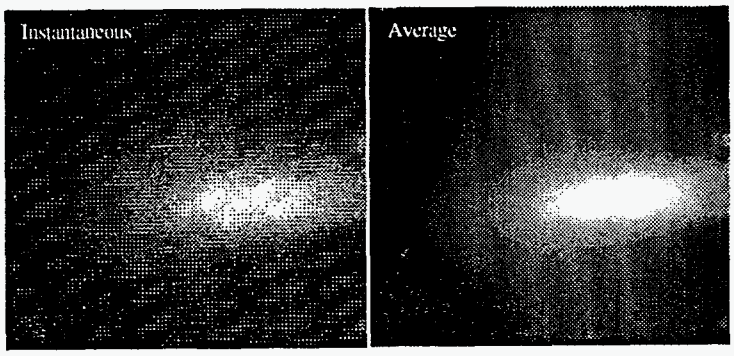

(b). With imposed acoustic field

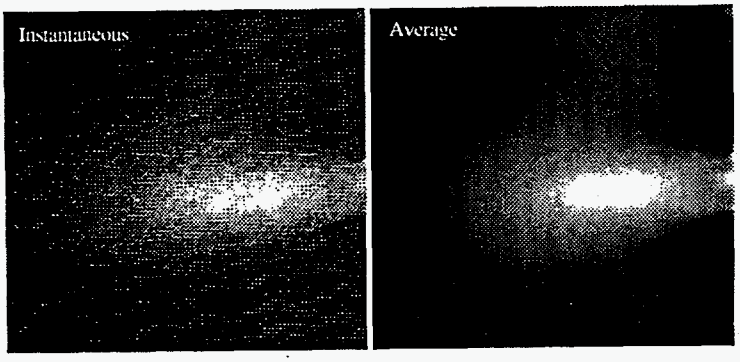

(c). No imposed acoustic field

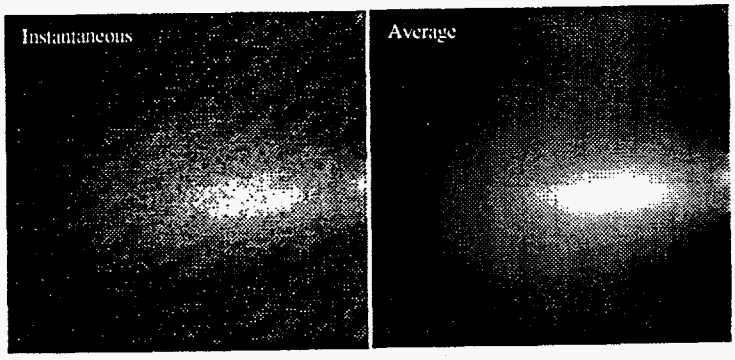

(d). With imposed acoustic field

Figure 15. Jet into cavity with partially closed exhaust end with no co-flow
(a), (b) With unrestricted co-flow inlet
(c), (d) With closed co-flow inlet

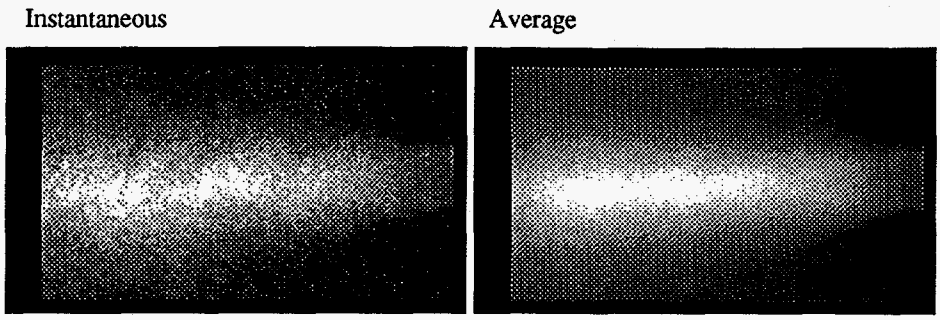

(a) No imposed acoustic field

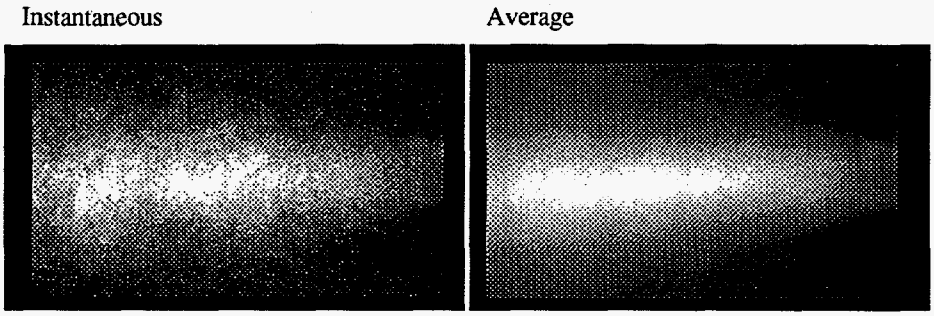

(b) With imposed acoustic field

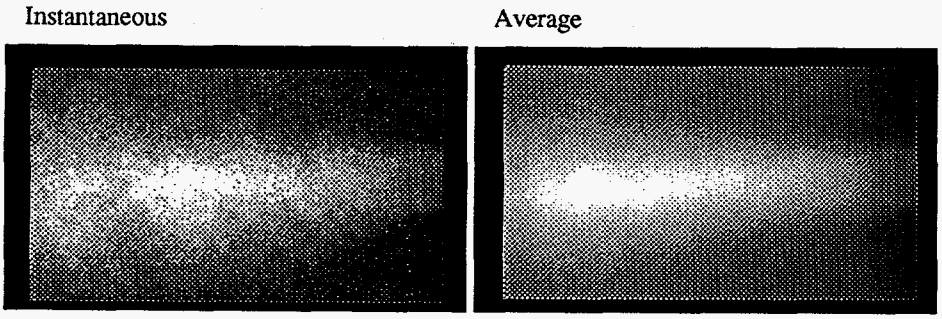

(c) No imposed acoustic field

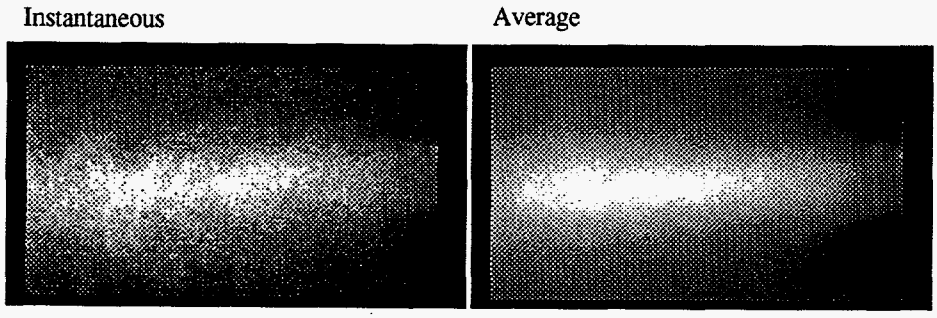

(d) With imposed acoustic field

Figure 16. Jet into cavity with unrestricted co-flow inlet with no co-flow
(a), (b) With no end nozzle
(c), (d) With end nozzle

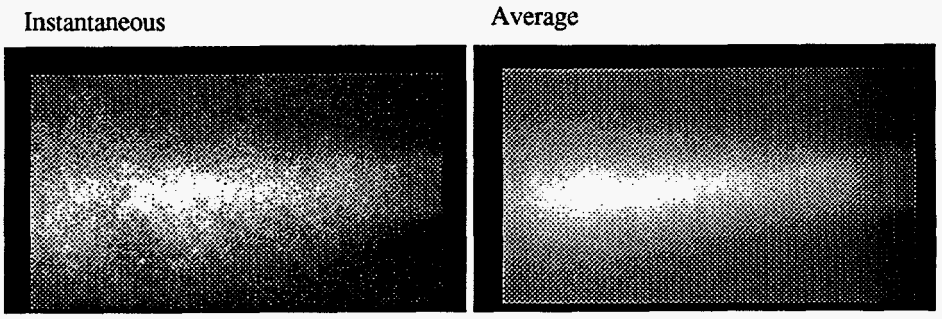

(a). No imposed acoustic field

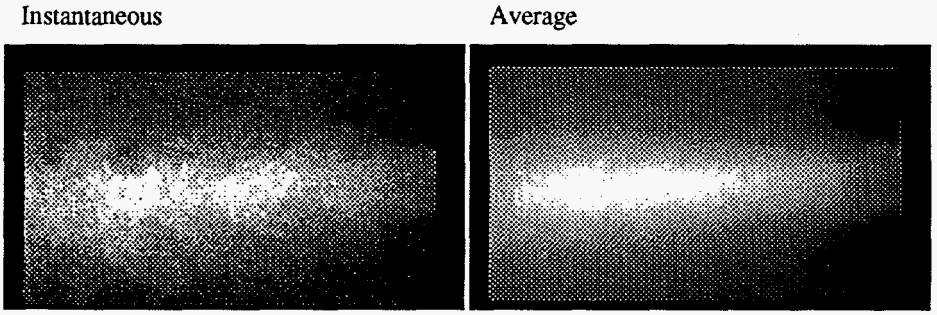

(b). With imposed acoustic field

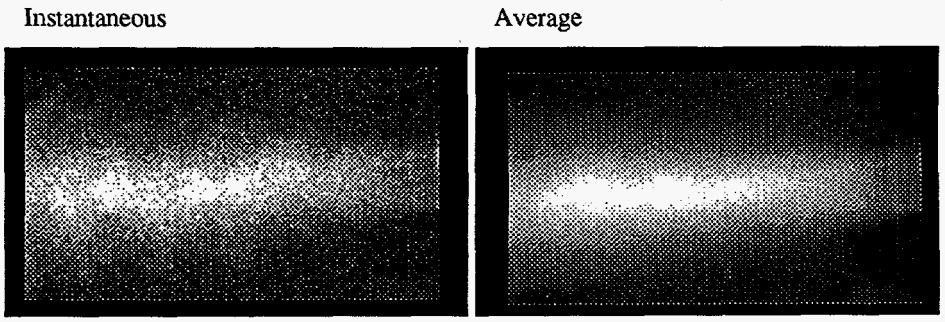

(c). No imposed acoustic field

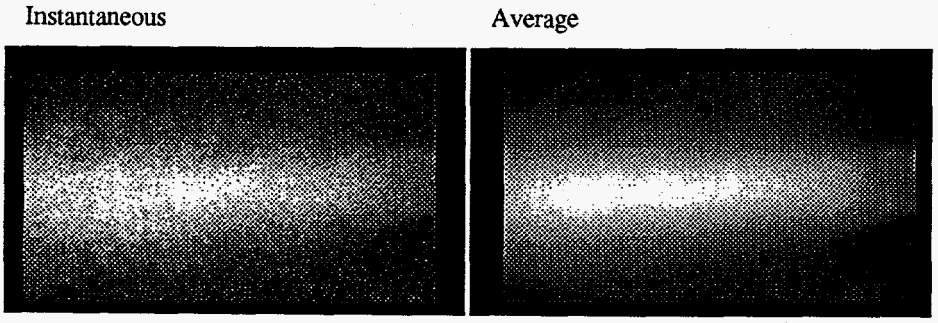

(d). With imposed acoustic field

Figure 17. Jet into cavity with unrestricted co-flow inlet with end nozzle
(a), (b) With no co-flow
(c), (d) With co-flow

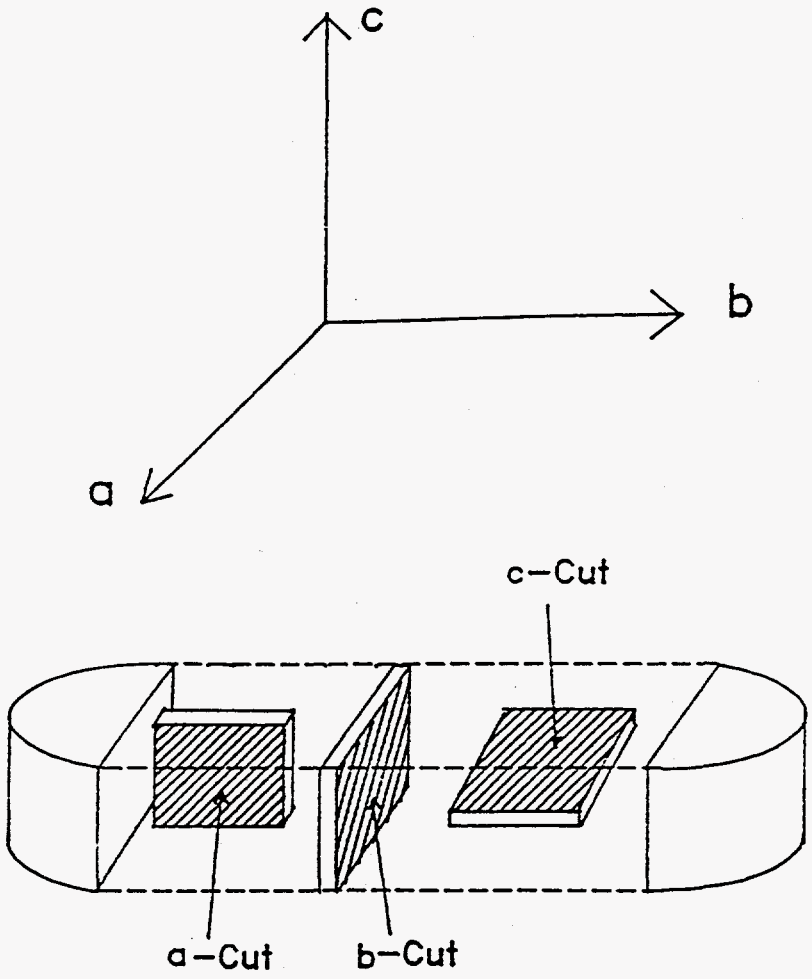

Figure 18. Cutting of grain oriented $Sr_2(Nb_xTa_{1-x})_2O_7$ ceramics (x = 1.0) fabricated by chemical coprecipitation method

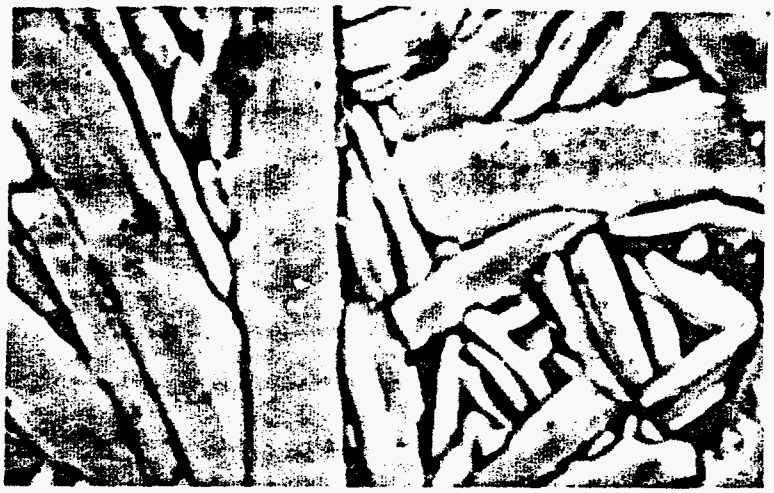

a-cut

b-cut

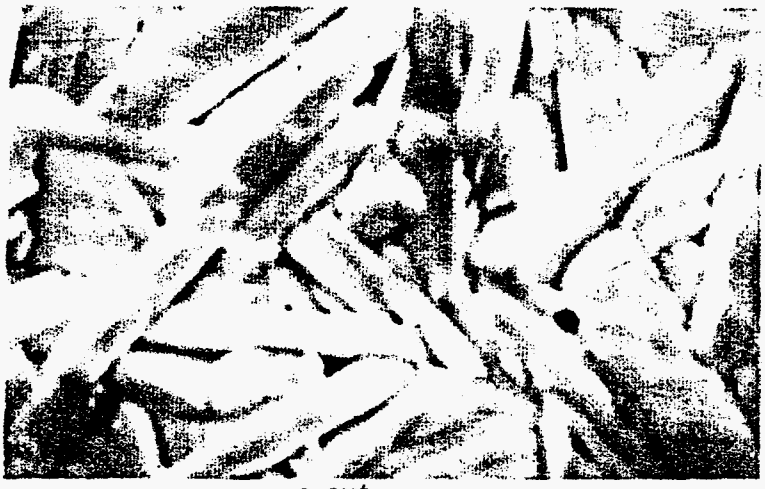

c-cut

Figure 19. SEM micrographs for sintered $Sr_2(Nb_xTa_{1-x})_2O_7$ ceramics (x = 1.0) cut along a-axis, b-axis, c-axis

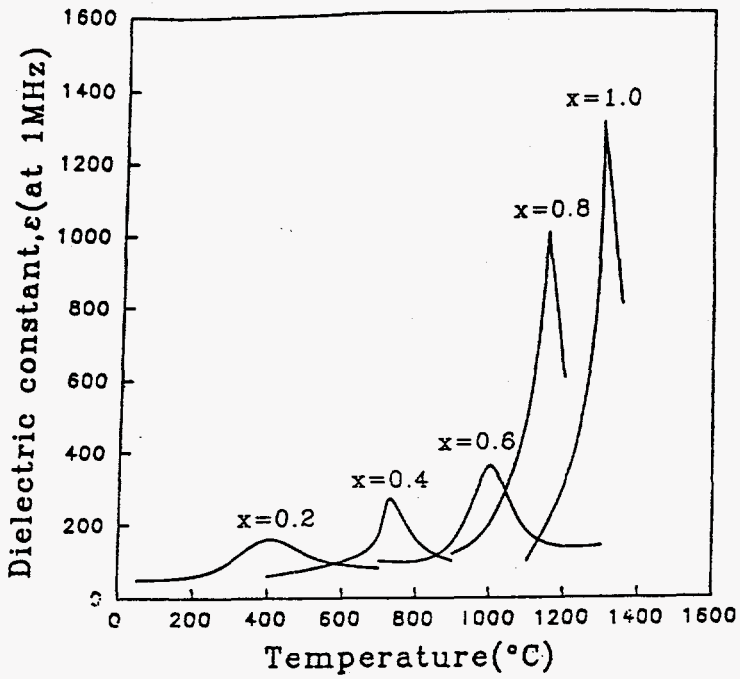

Figure 20. Temperature dependence of dielectric constant for $Sr_2(Nb_xTa_{1-x})_2O_7$ ceramics sintered at 1500 °C

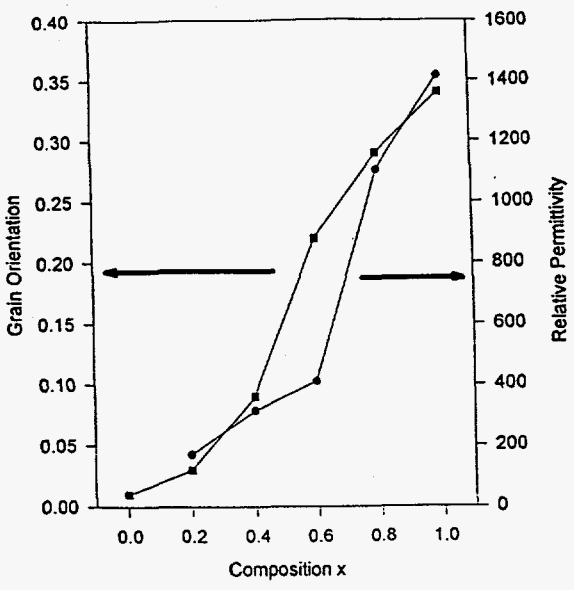

Figure 21. Relative permittivity at Curie temperature and grain orientation vs. composition x for $Sr_2(Nb_xTa_{1-x})_2O_7$ ceramics

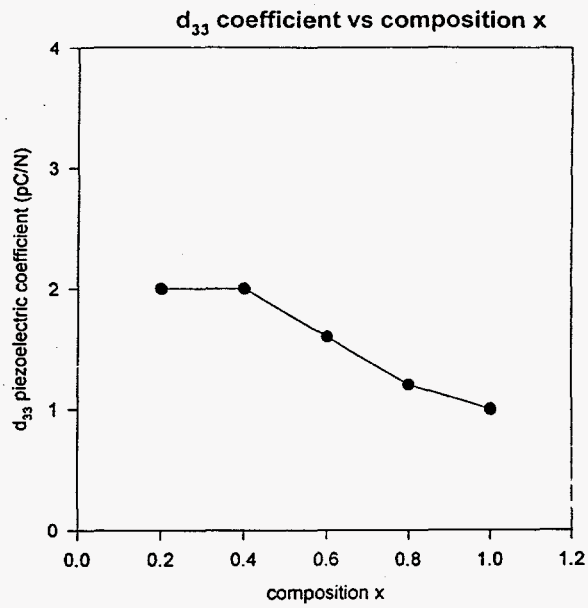

Figure 22. Compositional dependence of the d33 coefficient for $Sr_2(Nb_xTa_{1-x})_2O_7$ ceramics sintered at 1500 °C